

Introduction

Since May 2003, I have performed computer simulations of electromagnetic field effects for Professor Steven Anlage's research group at the University of Maryland's Center for Superconductivity Research. My work has supported the research of several individuals in Dr. Anlage's group, but this paper will focus on two efforts in particular: the study of left-handed materials and microwave microscopy.

The Anlage group performs computer simulations for two reasons. First, simulations help to predict results that researchers may expect from their experiments, which can provide them with a benchline against which to compare their results. For example, I conducted simulations to determine the refractive properties of a prism that were later verified experimentally. In addition, predicting results may provide researchers with greater insight into planned experiments so that they can make adjustments before investing considerable effort and resources in setting up and conducting the experiments. For example, I modeled how placing a thin conducting film above a dielectric substrate would affect the local electric field during microwave microscopy experiments, helping a researcher to understand these effects before deciding whether to use such a thin film in his own experiments.

Second, simulations can provide quantitative analysis of experiments for which it may be difficult to measure precise quantities experimentally. For example, it is important to maximize the spatial resolution of a microwave microscope, but it is often difficult to measure this property accurately in a laboratory setting. Software simulations can often provide quantitative results to assist researchers in their efforts.

Description of Ansoft Software

What the Software Can Do

I used two pieces of software produced by the Ansoft Corporation to simulate problems for the Anlage group: HFSS and Maxwell 2D (M2D).

HFSS

During my time with the Anlage group, I primarily used HFSS, which simulates time-dependent electromagnetic effects in three spatial dimensions. This software has several properties that make it well-suited for simulating the group's experiments.

First, projects may be solved using eigenmode or driven solutions. In the first case, when solving a project, the software finds its eigenmodes. The user may solve for only the lowest eigenmode (i.e., the one with the lowest resonant frequency) or several. This solution method is useful, for example, in determining the resonances of closed cavities. In the second case, when solving a project, the software determines properties of the system as electromagnetic radiation propagates through it. This method is useful, for example, in simulating transmission lines in which electromagnetic radiation enters from one end and exits from another.

Having specified a solution method, the user must design the model. He defines units of length and draws the model in three dimensions, and HFSS provides robust capabilities to customize the design. The model may include lines (including curved lines), 2-dimensional surfaces (including curved surfaces), and 3-dimensional objects.

Next, the user specifies the types of materials of which objects in the model are made. I typically used conductors (i.e., metals such as tungsten and copper), common dielectrics (such as silicon and teflon), and air and vacuum. HFSS includes preset properties for these materials, including electric permittivity, magnetic permeability, bulk conductivity, and dielectric loss tangent.

Next, the user may determine boundaries to be used along faces of model items and the outer boundary of the drawing area. For example, a user may define a boundary to simulate the existence of a perfect conductor along an object's face. Electromagnetic radiation striking the face will reflect perfectly, and electric field lines will be perpendicular to the face. Defining a "radiation boundary" simulates the existence of empty space along a face. Radiation striking that face will propagate without reflecting back into the model area (or simply be absorbed).

The user then defines ports and port excitations. Ports may be placed along faces of objects and serve as means for electromagnetic radiation to enter and exit the model. The excitation determines the frequency of the incoming radiation. Users may solve projects for incident radiation with a wide variety of frequencies very easily by defining "frequency sweeps." For example, a user may define a frequency sweep of 7 to 13 GHz in steps of .5 GHz, so that the model would first be solved for incident radiation with a frequency of 7 GHz, then 7.5 GHz, then 8 GHz, etc. until 13 GHz.

The next step is to define solution options. In order to solve a model, HFSS generates a mesh of tetrahedra in the space that the model occupies. HFSS solves the project using these tetrahedra as building-blocks. The software then determines the areas of the mesh in which the solution is poorest and creates a new mesh for the entire model with more tetrahedra, with most of the new tetrahedra being placed in the deficient area. HFSS then solves the model again, this time finding a more accurate solution. The software continues in this way for several passes. More accurate solutions are generated by meshes with more tetrahedra, and the user can define solution options that require the software to generate greater numbers of tetrahedra for the mesh. The tradeoff is that HFSS requires more time and computing power to find solutions for more refined meshes.

After a solution is computed, the user can display results in one of two methods. The first method is to generate a plot of the model's electric or magnetic fields. Color plots indicate the strengths of these fields, while vector plots indicate both magnitude and direction at representative points. Plots can also be animated to display the time-dependent behavior of these fields. The second display method is the generation of tables and graphs, such as scattering matrices and graphs of scattering matrix elements (such as S_{11}) vs. frequency or phase.

Maxwell 2D

The second piece of software that I used was M2D. This program solves Laplace's equation ($\nabla^2 V=0$, where V is the electrostatic potential) to determine time-independent solutions to electromagnetic problems.

As its name implies, M2D uses 2-dimensional models only. Therefore, in order to simulate an actual laboratory experiment, the model must have either plane or rotational symmetry. If the user selects plane symmetry, then Cartesian coordinates are used, the model is drawn in the x-y plane, and the model is assumed to have symmetry along the z-axis. (For example, the square in figure 1 would represent a box with infinite length in the z direction. In this model, the software represents the x and y axes as u and v. The hash-marks represent the origin of the coordinate system.) If the user selects rotational symmetry, then cylindrical

coordinates are used, the model is drawn in the r-z plane, and the model is assumed to have rotational symmetry about the z-axis. (For example, the square in figure 2 would represent a cylinder whose axis of symmetry lay along the z axis. In this model, the software represents the r and z axes as u and v.)

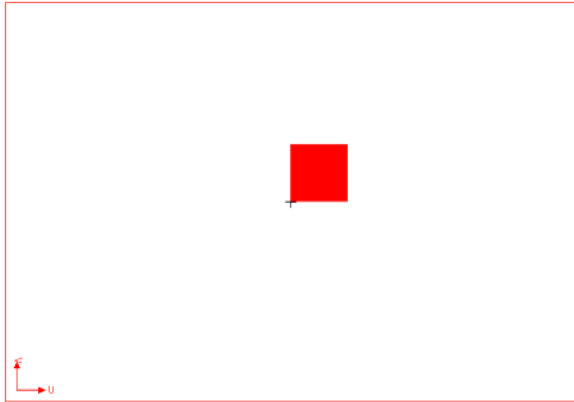


Figure 1. This model, with planar symmetry, represents a box infinitely long in the z-direction.

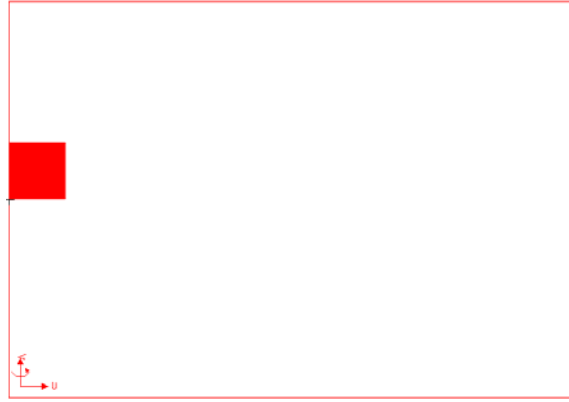


Figure 2. This model, with rotational symmetry about its left edge, represents a cylinder.

Once the user has drawn the model, he defines materials, boundaries, and solution options in a manner similar to how he would do so in HFSS.¹ (Ports and excitations are not defined since M2D only calculates static solutions.) The user can also generate plots of electric and magnetic field strengths, but tables and graphs are different, since scattering matrices can not be determined for static solutions. Instead, I usually determined capacitance matrices, which represent the capacitances among conducting objects in the model.

Shortcomings of HFSS, M2D

Despite the capabilities of HFSS and M2D, these software programs had several drawbacks. For example, the modeling capabilities had strict aspect ratio limits. Aspect ratio is defined as the ratio of the longest length-scale in the model to the shortest, and Ansoft recommends that this number not exceed 10^4 . I sometimes managed to get the software to run with larger aspect ratios, but when they became too large, either the results became erratic or the software simply failed to run.

Another problem was the failure of the software to mesh models properly on occasion. Sometimes tetrahedra would overlap, and sometimes their vertices would fail to coincide (i.e., the tetrahedra would not be adjacent, as required). I often did not know why these problems occurred. Instead, I had to rely on trial-and-error to make minor adjustments in the model and in order to determine what would work.

In addition, it was often impossible to calculate errors for numbers produced by HFSS and M2D. For example, it was sometimes impossible to determine whether numbers produced by the software (such as capacitances between objects or strengths of electric fields) were consistent

¹ The user determines the mesh refinement as he does in HFSS. However, the mesh consists of triangles, not tetrahedra, since M2D models are two-dimensional.

with observations from laboratory experiments. Although we could determine errors for these experimental results, we had no way of determining how accurate the software results were.

Left-Handed Materials

I simulated several projects for Michael Ricci and Nathan Orloff, two students in Dr. Anlage's group conducting experiments with left-handed materials (LHMs), which have negative indices of refraction (n). Victor Veselago provided the theoretical outline for the behavior of such materials in 1968,² but physicists only successfully created such materials in the late 1990s. Many researchers are now exploring the properties of these exotic materials, which may contribute to significant advances in optics and related fields.

Ricci's and Orloff's goal was to create an LHM object and demonstrate its negative index of refraction by creating a negative Goos-Hänchen shift. When a collimated incident electromagnetic wave strikes a plane separating one medium from another, it refracts according to Snell's law, so that $n_1 \sin(\theta_1) = n_2 \sin(\theta_2)$, where n_1 and n_2 are the indices of refraction of the incident and encountered media, respectively, and θ_1 and θ_2 are the angles between the beam and lines drawn normal to the plane of separation. When $\theta_1 = \sin^{-1}(n_2/n_1)$, then $\theta_2 = 90^\circ$ and the outgoing beam travels along the plane of separation. When the incident angle exceeds this critical value, then the outgoing beam reflects back into the incident medium, but it does so from a point that is displaced from the point at which it struck the plane. This lateral displacement is the Goos-Hänchen shift. (See figure 3.) When the encountered medium has a negative index of refraction, the Goos-Hänchen shift should be in the direction opposite to that of materials with positive indices of refraction.³

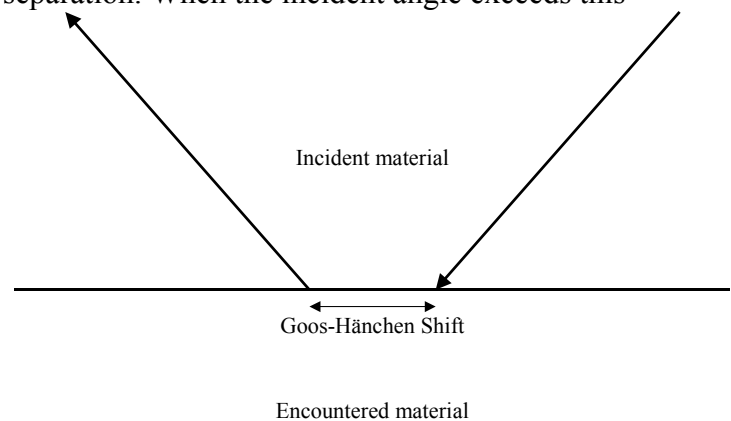


Figure 3.

Waveguide Simulation

Ricci and Orloff wanted to use a waveguide to direct incident microwaves toward their apparatus, and one early concern was that they might excite a mode of higher order than the waveguide's lowest mode for the propagating wave. In order to test this idea, I created a model of a simple three-dimensional box in HFSS, 12" long and with a standard X-band cross-section (.4" x .9"), to represent the waveguide. The incident port was placed at one end of the waveguide, and an outgoing port was placed at the opposite end. Ricci and Orloff used metal plates to form the top and bottom of their waveguide, so I set the boundary conditions on the top and bottom faces of my HFSS waveguide to simulate perfect conductors. They also placed a material especially designed to absorb microwaves along the sides of their waveguide, so I gave

² V. G. Veselago, "The Electrodynamics of Substances with Simultaneously Negative ϵ and μ ," *Sov. Phys. Usp.* 10, no. 4 (Jan-Feb 1968): 509-514.

³ Ilya V. Shadrivov *et al.*, "Giant Goos-Hänchen Effect at the Reflection from Left-Handed Metamaterials," *Applied Physics Letters* 83, no. 13 (29 September 2003): 2713-2715.

the sides of the HFSS waveguide a radiation boundary condition to simulate the effect of having the wave strike the sides and simply disappear (“radiate” away).

I first ran the simulation with the frequency of the incident wave set to $f=13$ GHz. A plot of the magnitude of the electric field revealed that the lowest-order mode was excited, as we expected. (See figure 4.)

Next, I changed the boundary conditions on the sides of the waveguide to simulate perfect conductors instead of radiation boundaries, so that all four faces parallel to the direction of propagation simulated perfect conductors. The electric field plot indicated that a higher-order mode was excited, also as expected. (See figure 5.) This result had no direct relevance to Ricci’s and Orloff’s experiment, since the sides of their waveguide would always be covered with microwave absorber, but it did confirm that HFSS was calculating the electric fields as we expected it to.

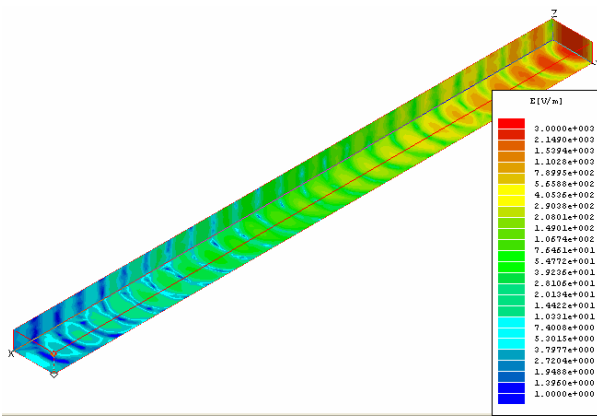


Figure 4.

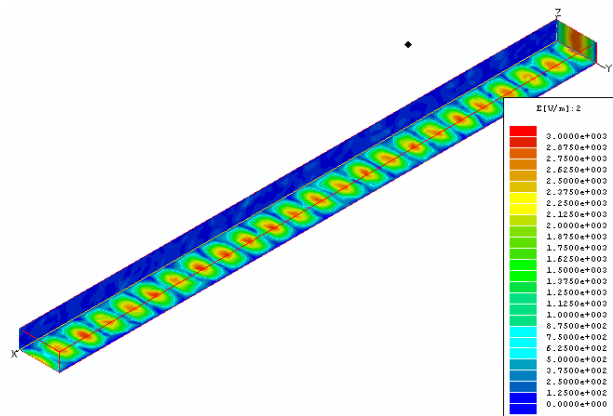


Figure 5.

Ricci and Orloff were concerned that they might excite higher-order modes if they increased the height of their waveguide to more than .4”, so I ran projects with heights of .4”, .8”, .9”, and 1”. I ran the projects at a frequency of 10 GHz, since Ricci and Orloff were interested in using microwaves with frequencies between 7 and 13 GHz. The results at .4” were similar to those in figure 4; the wavefronts were spaced further apart due to the lower frequency, but otherwise the plots appeared similar, indicating that the lowest-order mode was still being excited. (See figure 6.) The results at .8” also indicated that the lowest-order mode was being excited. (See figure 7.) However, at .9” the structure of the electric field changed dramatically at the end of the waveguide nearer to the incident port, indicating that a higher-order mode was becoming excited. (See figure 8.) At 1” the new mode appeared to have completely replaced the lowest-order mode. (See figure 9.)

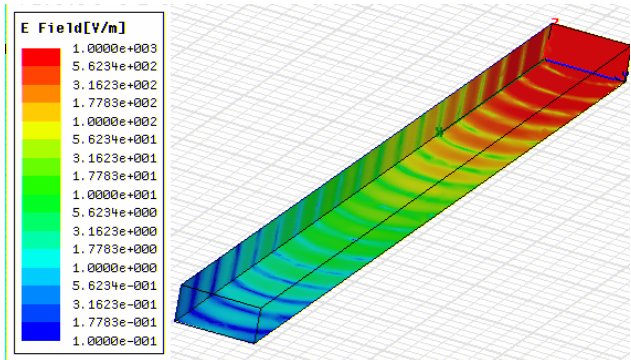


Figure 6. $z=.4''$, $f=10$ GHz.

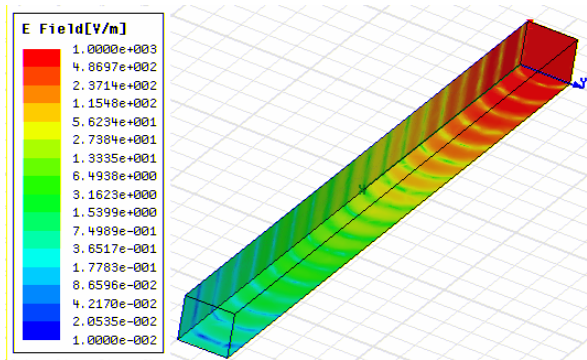


Figure 7. $z=.8''$, $f=10$ GHz.

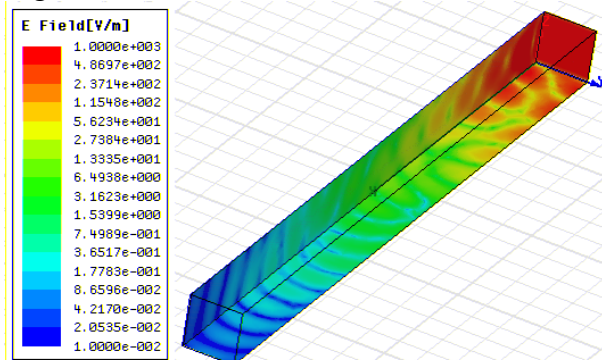


Figure 8. $z=.9''$, $f=10$ GHz.

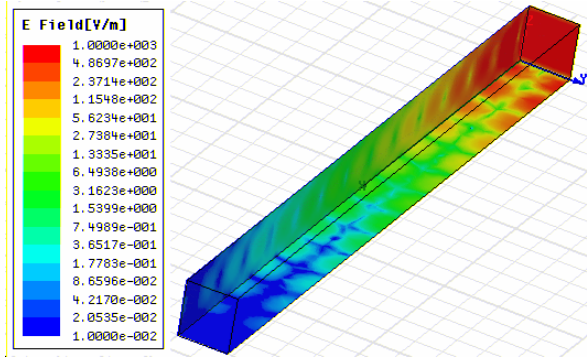


Figure 9. $z=1''$, $f=10$ GHz.

Ricci and Orloff ultimately decided to set the height of the top surface of their apparatus at a little less than $.5''$. Although I only ran simulations at 10 GHz, I did not see any higher-order mode in my simulations until the height exceeded $.8''$, so Ricci and Orloff felt comfortable that they would only excite the lowest-order mode if they kept the height below $.5''$ for microwave frequencies between 7 and 13 GHz.

Prism Refraction

Ricci and Orloff began to conduct experiments with a teflon prism, and I ran a series of simulations in support of that effort. These simulations had two purposes; the first was to determine the angle of refraction produced by the prism, in order to ensure that the refraction calculated by HFSS was consistent with what we expected based on theoretical calculations, and the second was to examine the refracted wavefronts emanating from the prism in order to ascertain how Ricci and Orloff could best measure the waves as they exited their apparatus.

My plan was first to design a simple apparatus, including only a waveguide and a cavity, and then add the prism and modify the geometry later. In my initial model, I created a $5.553'' \times 1.3315''$ waveguide attached to a $6'' \times 12''$ cavity, both of which contained only vacuum. (See figure 10.) The height of the entire model was $.4''$. The top and bottom surfaces were assigned perfect conductor boundary conditions, and all sides were assigned radiation boundary conditions with the exception of the far end of the waveguide, which was the source of the incident microwaves. (I had trouble making two segments of the cavity's walls into radiation boundaries, so I had to create thin "wings" along those edges in order to do so. The wings contained only vacuum and had no direct effect on the project.)

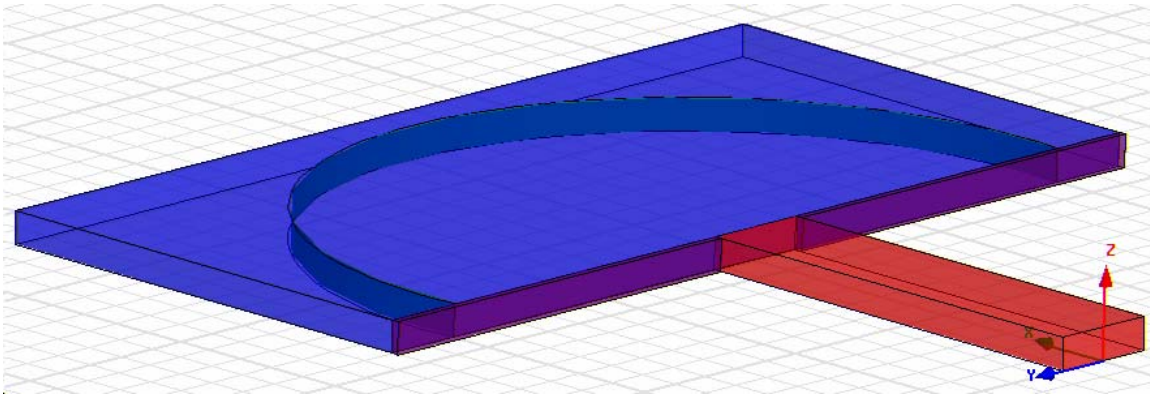


Figure 10. The initial setup for my prism refraction experiments. The waveguide is red, the cavity is blue, and the wings are purple.

We expected the incident waves to pass through the waveguide and enter the cavity, undergoing diffraction at the interface and propagating outwards to the cavity's walls, at which point they would be absorbed by the radiation boundary conditions there. Inside the cavity I created a semicircular "arc" centered on the midpoint of the aperture between the waveguide and the cavity. The arc was actually a two-dimensional curved strip that had no practical effect on the project. However, Ricci and Orloff planned to place detection devices at positions roughly along the path of this arc, and creating it allowed me to calculate the magnitude of the electric field along it so that I could predict what results Ricci and Orloff could expect from their detection devices.

I ran the project and plotted the magnitude of the electric field along the bottom surface of the apparatus and along the arc. (See figure 11.) Two points were of interest. First, the wave attenuated as it propagated and underwent diffraction upon passing from the waveguide into the cavity, as expected. Second, the magnitude of the electric field varied along the arc (i.e., the microwave radiation arrived at points along the arc with different phases), suggesting that the wavefront was not entirely circular. This result persuaded Ricci and Orloff not to place their detectors along the path of the arc but instead to find another method to detect the exiting microwaves.

Next I inserted a rectangular teflon prism ($\epsilon_r=2.56$, $\mu_r=1$, $n=1.6$) between the waveguide and the cavity.⁴ (See figure 12.) The new dimensions of the waveguide were 4.9" x 1.3214", the dimensions of the prism were 1.1568" x 3.6316", and the dimensions of the cavity remained 6" x 12". The electric field plot revealed several similarities between this project and the previous one: the wave attenuated as it propagated along the waveguide and in the cavity, it underwent diffraction at the aperture between the waveguide and the prism (and probably at the interface between the prism and the cavity, as well, although this effect was more difficult to see), and the wavefront arrived at the arc at various phases. (See figure 13.)

⁴ Throughout these experiments, I always set μ_r of the incident medium equal to 1.

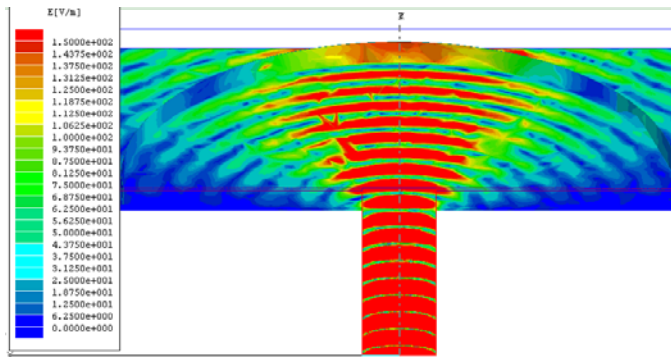


Figure 11.

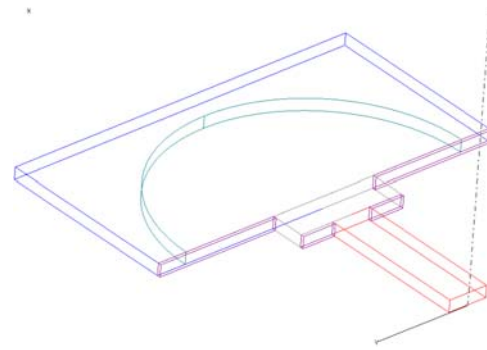


Figure 12.

However, one result was strikingly dissimilar to those of the previous project: the electric field displayed some unusual patterns inside the prism, and the wave actually appeared to strengthen during much of the time that it spent in this region. (This result is difficult to see in figure 13 but is clear when the plot is animated in HFSS, revealing how the electric field fluctuates and the wave propagates in time.)

This result is likely due to the superposition of the incident wave, traveling from the waveguide toward the cavity, and a reflected wave, traveling from the interface between the prism and the cavity (from which it is reflected) toward the aperture between the prism and the waveguide. Discovering this result was reassuring, since it indicated that HFSS could account for waves reflected from the interface between different media and calculate the superposition of waves traveling in different directions.

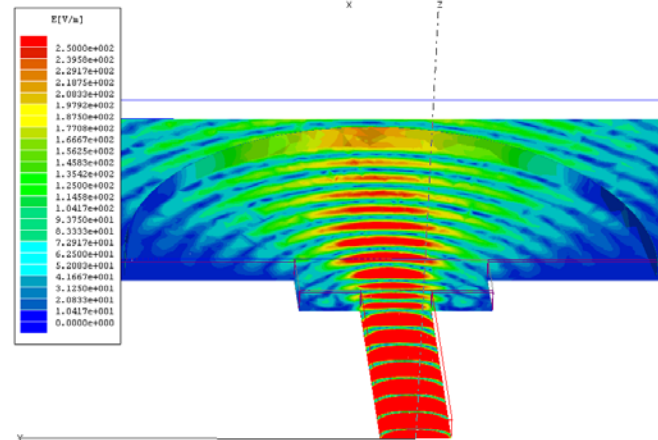


Figure 13.

For the next project, I modified the shape of the prism so that the interface between the prism and the cavity formed an angle of 17.5° with its previous orientation, mimicking the setup of a new experiment that Ricci and Orloff were interested in conducting. (See figure 14.) The resulting plot of the electric field makes it clear that the wave refracts upon exiting the prism. (See figure 15.) (The wave is also affected by refraction inside the prism, since the wave is partially reflected from the angled surface.) Using Snell's law, it is possible to determine the index of refraction of the prism from the angle of refraction (ignoring the effects of the reflected wave): $n_1 = n_2 \cdot \sin(\theta_2) / \sin(\theta_1) \approx \sin(\theta_2) / .3$, where n_1 is the index of refraction of the prism, $n_2 = 1$ is the index of refraction of the cavity, θ_2 is the angle that the outgoing wave makes with the line normal to the surface between the prism and the cavity, and $\theta_1 = 17.5^\circ$ is the angle that the incoming wave makes with that line. Since $n = (\epsilon_r \mu_r)^{.5}$, $\epsilon_{r1} = \mu_{r1} \cdot n_1^2 \approx (\sin(\theta_2) / .3)^2$. Orloff measured θ_2 and determined that ϵ_{r1} was approximately 2.28, which is not far from the value used for teflon in HFSS (2.56). Although Orloff did not tell me what the error of his calculation might have been, I imagine that it would have been quite significant, since it is not easy to measure θ_2 accurately from the plots in figure 15.

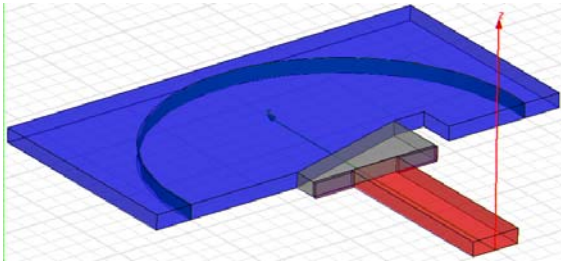


Figure 14. The shape of the prism allows the wave to be refracted at the interface between the prism and the cavity. The indentation to the right of the prism represents an area in which microwave absorber would be placed in order to absorb any microwaves exiting from the side of prism.

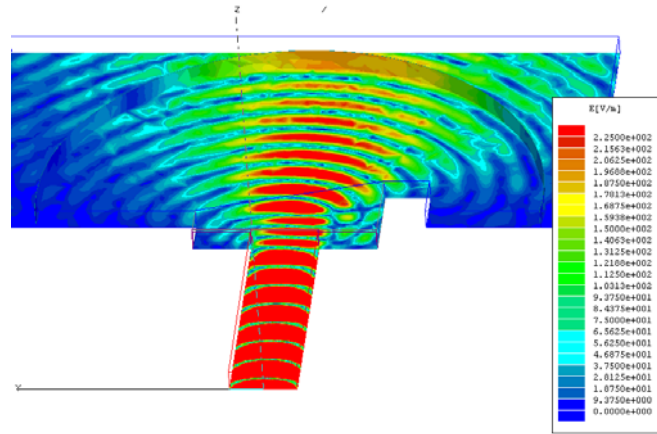


Figure 15. This electric field plot indicates that the wave undergoes refraction upon encountering the angled front edge of the prism.

Goos-Hänchen Shift

Next I conducted experiments to support Ricci's and Orloff's efforts to measure the Goos-Hänchen shift for left-handed materials. Their goal was for the wave to travel via a waveguide into a triangular prism, undergo total internal reflection inside the prism, resulting in a Goos-Hänchen shift, and then exit the prism at a location displaced from the location at which it would have exited had there been no Goos-Hänchen shift. In conducting these simulations, I varied the properties of the prism and surrounding media and simulated effects for frequencies between 7 and 13 GHz.⁵

First I created a model including a 10 cm x 12 cm waveguide, a triangular teflon prism ($\epsilon_r=2.2$, $n \approx 1.5$) measuring 24 cm along each side, a small cavity (cavity 1), and a large cavity (cavity 2). (See figure 16.) The top and bottom of the model are perfect conductors. The upper-left face of the waveguide represents the incident port, while the upper-right face of the prism is assigned a perfect conductor boundary condition. All other faces are defined as radiation boundaries, allowing radiation incident upon them to disappear. All objects except the prism contain only vacuum.

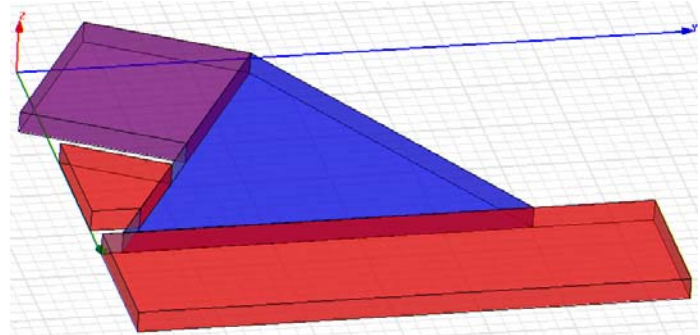


Figure 16. The waveguide is purple, the prism is blue, and the two cavities are red. The upper-left face of the waveguide is the incident port, and the upper-right face of the prism is assigned a perfect conductor boundary condition.

The wave was to pass through the waveguide and enter the prism along a path perpendicular to the interface between those media. The wave would then strike the back face of the prism, reflecting at the same angle at which it arrived. It would then pass into cavity 2,

⁵ For the sake of brevity, I primarily present electric field plots only for the case of $f=10$ GHz.

traveling along a path normal to the plane of separation. (See figure 17.) The purpose of this project was to serve as a control, since we knew exactly what to expect from the exiting wave.

The results for this project appear to confirm our expectations. (See figure 18.) The angles of incidence and reflection appear to be 60° . There appear to be many secondary wavefronts, probably due to the reflection of the incident wave from corners.

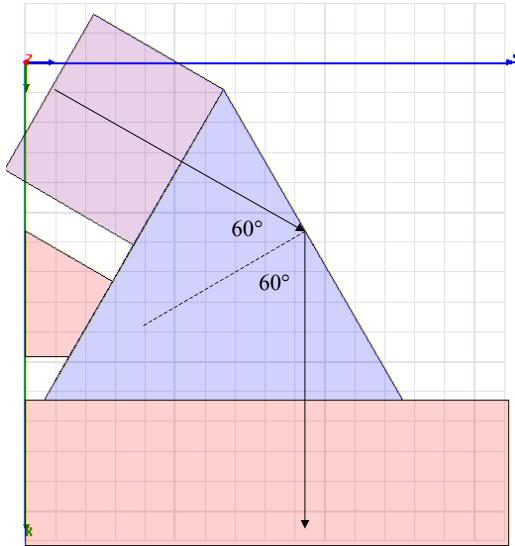


Figure 17. The wave's expected path with a perfectly conducting wall.

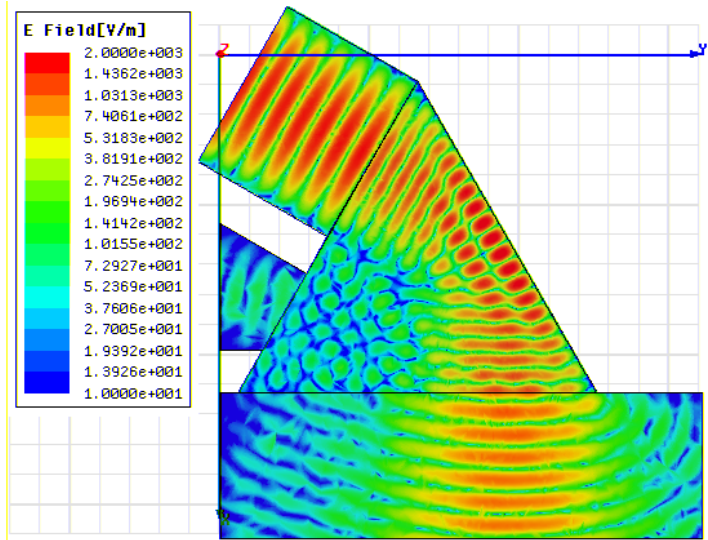


Figure 18. Results with a perfectly conducting wall, $\epsilon_r=2.2$, and $f=10$ GHz.

Next I added another cavity (cavity 3) behind the rear face of the prism, eliminating the perfect conductor boundary condition and defining the exterior faces of cavity 3 as radiation boundaries. (See figure 19.) With this setup, I could modify the index of refraction of the prism and of cavity 3 to achieve total internal reflection. This condition occurs when $n_2/n_1 = \sin(\theta_1) = \sin(60^\circ) = 3^{-5}/2 \approx .87$.

First I let $\epsilon_r=2.2$ so that $n_1 = \epsilon_r^{.5} \approx 1.48$ and $n_2/n_1 \approx 1/1.48 \approx .68 < .87$, creating total internal reflection. (See figure 20.) According to theory, after reaching the interface between the prism and cavity 3, the wave should travel along the interface (down and to the right, in figure 20) and then reflect, resulting in a Goos-Hänchen shift to the right. The wave does appear to travel for a short distance along the interface, and when figures 18 and 20 are printed on transparencies and overlaid, it is clear that the position of the outgoing wave has shifted to the right.

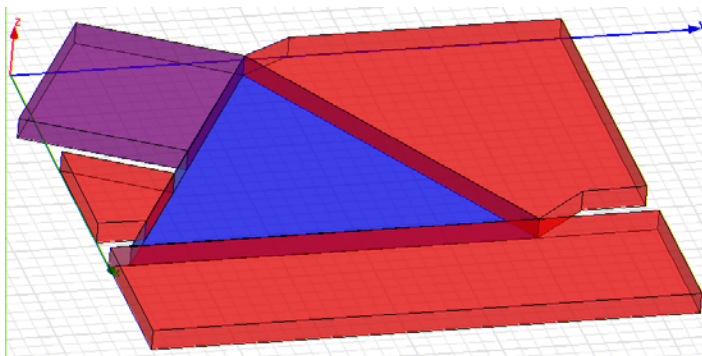


Figure 19.

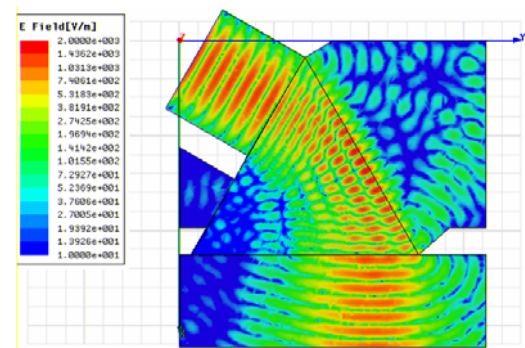


Figure 20. A field plot with $n_1 \approx 1.48$ and

$n_2=1$ for $f=10$ GHz.

For the next project, I let $\epsilon_{r1}=1.35$ so that $n_1=\epsilon_{r1}^{.5}\approx 1.16$ and $n_2/n_1\approx 1/1.16\approx .86<.87$, again creating total internal reflection. (See figure 21.) Two points are interesting in this case. The first is that n_2/n_1 is only barely less than $\sin(\theta_1)$, so the total internal reflection is actually not complete (due to imperfections in the simulation such as corner effects). The result of this is clear in figure 21, where some of the wave that is supposed to be traveling along the interface between the prism and cavity 3 actually “leaks” into cavity 3 at a shallow angle. The other point is that theory predicts that the Goos-Hänchen shift should be more pronounced when the critical angle nears the incident angle. In this case, the critical angle is $\theta_1=\sin^{-1}(n_2/n_1)=\sin^{-1}(1/1.16)\approx 59.55^\circ$, which is quite close to the incident angle $\theta_1=60^\circ$, and by comparing figures 21 and 20 it is clear that the Goos-Hänchen shift is much more pronounced in this case than previously.

Next I set ϵ_{r1} back to 2.2 but modified the relative permittivity of cavity 3 to $\epsilon_{r2}=-1$ and its relative permeability to $\mu_{r2}=-1$. I was trying to achieve $n_2=-1$, which should still yield total internal reflection since the criterion when n_2 is negative is that $|n_2/n_1|<\sin(\theta_1)$. This would be true in this case, since $|n_2/n_1|\approx |-1/1.48|\approx .68<.87$. Still, I was not sure of how to achieve $n=-1$ in HFSS, but the results were encouraging. (See figure 22.) The simulation appears to display total internal reflection (ignoring some stray waves in cavity 3 that appear to emanate from the corners of the prism and are probably due to corner effects), and the Goos-Hänchen shift is clearly in the direction opposite to its earlier direction (i.e., the outgoing wave is now shifted to the left instead of to the right).

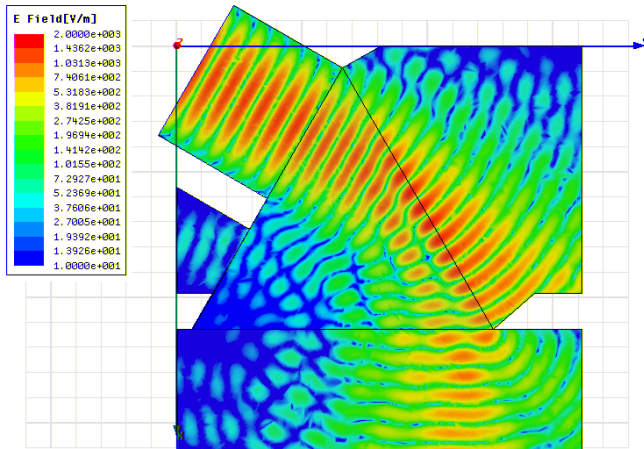


Figure 21. A field plot with $n_1\approx 1.16$ and $n_2=1$, creating total internal reflection, for $f=10$ GHz.

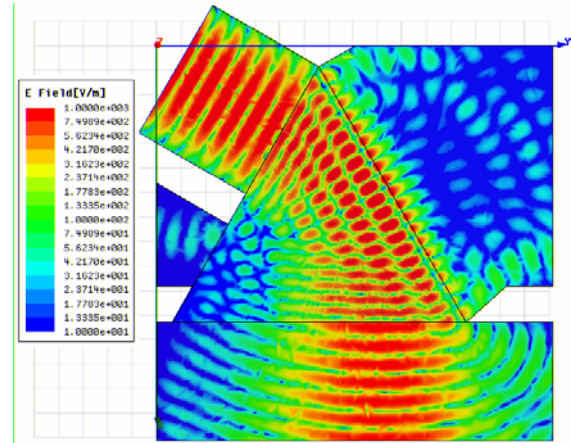
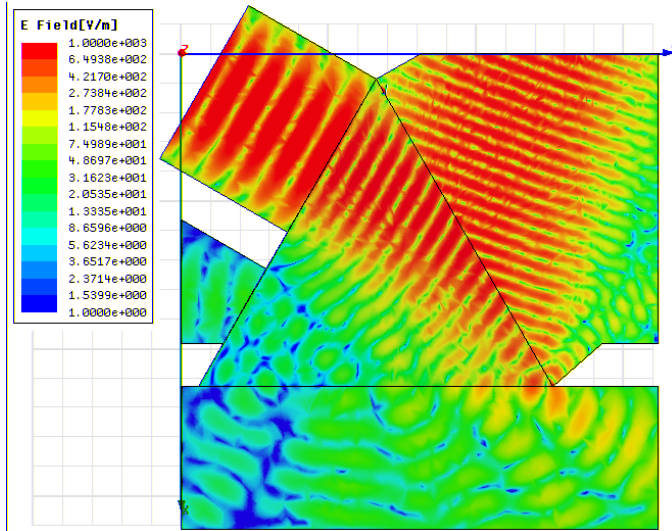


Figure 22. A field plot with $n_1\approx 1.48$ and $n_2=-1$, creating total internal reflection and a negative Goos-Hänchen shift, for $f=10$ GHz.

Finally, I let $\epsilon_{r1}=2.2$, $\epsilon_{r2}=-2$, and $\mu_{r2}=-2$. I was trying to achieve $n_2=-2$, in which case there would be no total internal reflection since $|n_2/n_1|\approx |-2/1.48|\approx 1.35>.87$. The simulation results agreed with this prediction, since the electric field plot displayed a reflected wave in cavity 3. (See figure 23. Note that this figure is plotted at a frequency that is different than those of Figure 23. A field plot with $n_1\approx 1.48$ and $n_2=-2$, creating a reflected wave that travels in the direction opposite to the direction seen in ordinary materials,

earlier plots.) The reflected wave was also on the same side of the normal to the plane separating the media as the incident



for $f=8$ GHz.

wave, which would only be true if one of the materials had a negative index of refraction. Furthermore, I animated the field plot, and the reflected wave propagated *toward* the plane separating the media. The incident and reflected wave, in fact, acted as if the plane separating them were a mirror: both waves approached the plane from the same side of the normal, and they appeared to annihilate each other upon meeting at the plane. Therefore, I felt very confident that HFSS was in fact simulating a left-handed material and that this method could be used to support further LHM experiments.

Conclusion

As a result of these experiments, I came to several conclusions. First, I determined that no higher-order mode was excited in the waveguide for $f=10$ GHz until the height of the apparatus reached at least .8", which was significantly greater than the height that Ricci and Orloff used. Second, my results from the prism refraction experiment indicated that HFSS appeared to simulate the refraction properly. Third, I determined that HFSS could simulate left-handed materials correctly. Finally, I showed that the Goos-Hänchen shift could be produced in HFSS, demonstrating the effect of left-handed materials and assisting other researchers in designing and conducting their own experiments in this field.

Microwave Microscopy

Most of my work in Dr. Anlage's group has been in support of Atif Imtiaz's microwave microscopy experiments. Imtiaz's microscope includes a probe that hovers a very small distance (typically between one nanometer and a couple of microns) above a sample film. A microwave signal is directed from the probe's tip to the sample and interacts with the sample. By studying the return signal, Imtiaz can characterize the sample's properties.

The purpose of this kind of microscopy is to determine the properties of various materials on a very small scale. Similar techniques may be useful in the burgeoning field of nanotechnology. In order to design nanoscale devices, physicists and engineers need to determine various properties of these materials such as their inductances and resistances. Because of the devices' small size, standard characterization techniques are often inadequate, and designers must rely on more specialized methods, such as microwave microscopy.

Microwave Microscope Geometry

Imtiaz asked me to simulate field effects in the neighborhood of a microwave microscope probe tip and sample. The objective of this work was to optimize the design of the probe tip to maximize its sensitivity to properties of the sample very near the tip (i.e., its spatial resolution).

The “business end” of Imtiaz’s microscope includes a solid conducting cylinder and a hollow conducting cylinder. The cylinders are coaxial, sharing a central axis aligned vertically. Near the bottom of the apparatus, the inner conductor (the probe) extends below the outer conductor before ending in a conical tip. This tip is suspended a small distance above the sample, and the height of the arrangement (“h”) is defined as the distance between the sample surface and the tip. Microwave radiation propagates downward along the coax, interacts with the sample, and returns along the coax. Imtiaz measures the returning wave in order to determine properties of the sample. Imtiaz was interested in simulating the operation of his microscope and microscopes of somewhat different geometries in order to determine whether he could improve the spatial resolution of his experiments.

Validation Effort: Capacitance of Coaxial Conductors

During the early stages of this project, Dr. Anlage noted that it was important to determine whether M2D really calculated capacitances as we expected it to. I therefore modeled the coaxial part of Imtiaz’s microscope, ignoring the tip below. Imtiaz used a standard 085 coaxial cable, with an inner conductor with radius 127 μm and an outer conductor with inner radius 840 μm and outer radius 1080 μm. I modeled these two conductors as purple and brown rectangles in M2D, respectively, letting the left edge of the drawing area represent the axis of rotational symmetry. (See figure 24.)

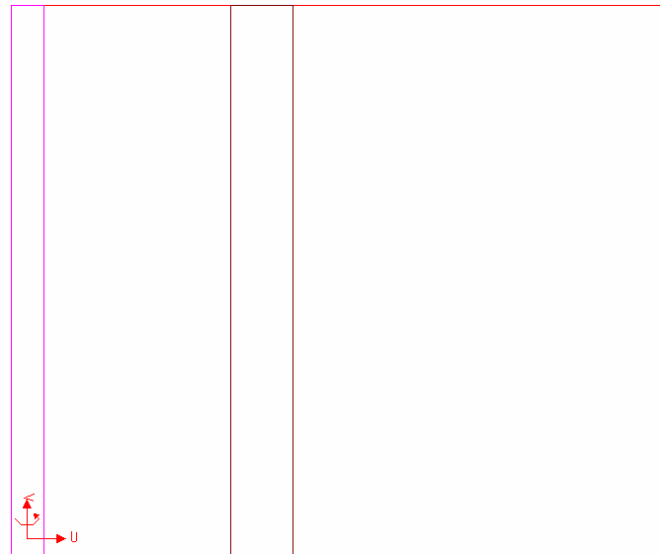


Figure 24.

Letting the radius of the inner conductor be a, the inner radius of the outer conductor be b, the length of the entire section (i.e., the height of the drawing area) be l, and the relative electric permittivity of the area inbetween the two cylinders be ε_r, the analytic solution for the capacitance between the conductors is given by $C=2*\pi*\epsilon_0*\epsilon_r*l/\ln(b/a)$.⁶ I entered appropriate values for these variables in the software program Excel, which provided the following solution.

l (m)	a (μm)	b (μm)	ε ₀ (F/m)	ε _r	C (F)
0.0021	127	840	8.8542E-12	1	6.18397E-14

M2D calculated the capacitance between the conductors to be 6.184x10⁻¹⁴ F. Although it was not possible to estimate the error of this calculation, Dr. Anlage, Imtiaz, and I believed that

⁶ Simon Ramo *et al.* *Fields and Waves in Communication Electronics*. New York: John Wiley & Sons, 1994, pg. 250.

the result demonstrated that M2D could calculate capacitances to a degree of accuracy that was adequate for our work.

Theoretical Approach to Microscope Tip with Three Capacitors

Imtiaz's microscope may be thought of as a system of three capacitors: one between the probe and outer conductor (C_{p-o}), one between the outer conductor and the sample (C_{o-s}), and one between the probe and the sample (C_{p-s}). (See figure 25.)

Because the electromagnetic radiation originates from and returns to an area above the apparatus, C_{p-o} is essentially connected in parallel to C_{p-s} and C_{o-s} , which are connected in series with each other. Therefore, it is reasonable to define a sample capacitance C_s so that $C_s = (1/C_{p-s} + 1/C_{o-s})^{-1}$.

Imtiaz had two objectives in order to improve the spatial resolution of his microscope. First, in order to localize the electric field near the tip, he wanted stronger fields between the probe and sample than between the outer conductor and the sample. Therefore, he wanted C_{p-s} to be much less than C_{o-s} , since lower capacitance between two conductors implies a stronger electric field between them. At the same time, he wanted to ensure that more of the incident wave was traveling through the sample than between the probe and outer conductor. Therefore, he wanted Z_s to be much less than Z_{p-o} , where Z_s is the sample impedance and Z_{p-o} is the impedance between the probe and the outer conductor. Finding a new microscope geometry that would satisfy both of these conditions was a key goal of this set of simulations.

Simulation with Imtiaz's Microscope Geometry

In order to model Imtiaz's microscope I drew three objects in M2D. (See figures 26 and 27.) First I drew the probe (the purple object) along an axis of rotational symmetry, letting its radius (above the conical taper) be $127 \mu\text{m}$. Next I drew the outer conductor (the brown object at the top of the drawing area) so that its inner radius was $840 \mu\text{m}$, its outer radius was $1080 \mu\text{m}$, and its bottom edge was $800 \mu\text{m}$ above the probe's tip. (I called this distance, representing the extension of the probe tip beyond the outer conductor, "x.") Finally, I drew the sample (the green object) below the probe. The probe is touching the sample in figures 26 and 27, but I assigned the variable d_{left} to represent the sample's height and modified this variable so that h (the distance between the sample and the probe tip) assumed a range of values.

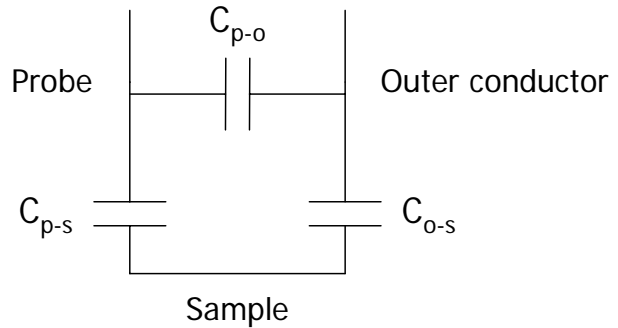


Figure 25.

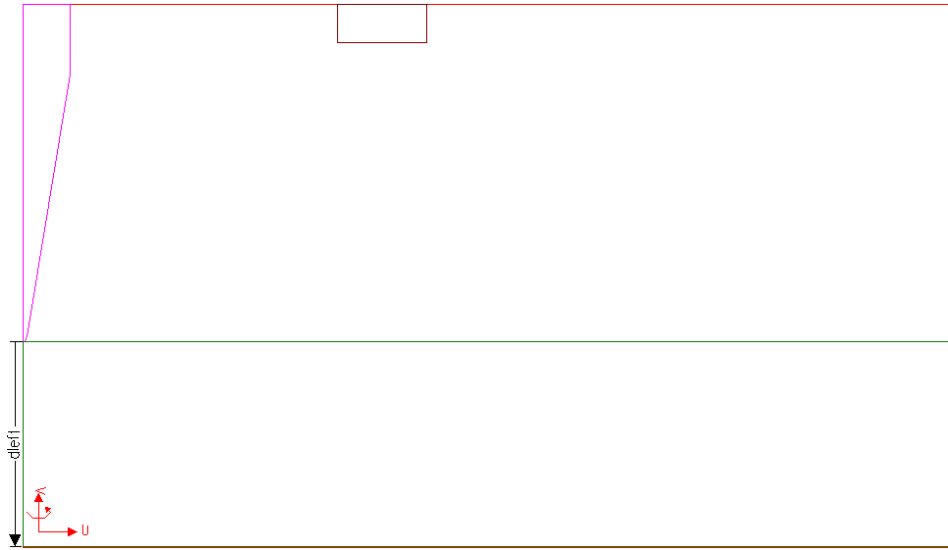


Figure 26. A model of Imtiaz's microwave microscope with $x=800 \mu\text{m}$. The probe is the pink object along the left edge of the model (the axis of rotational symmetry), the outer conductor is the brown object at the top, and the sample is the green object at the bottom of the model.

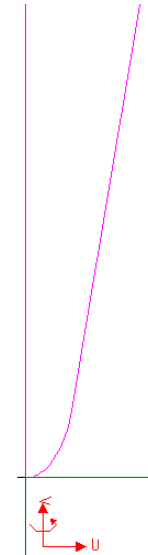


Figure 27. This is a detail of figure 26, showing the area in which the probe tip and sample surface meet.

I assigned all three objects to be made of metals. I let the voltage on the probe be 1 V and the voltage on the outer conductor be 0 V, and I let the sample float (with no charge assigned to it). I ran the project for values of h from 0 to $2 \mu\text{m}$ and created a vector plot of the electric field for $h=.5 \mu\text{m}$, which appeared to be similar to what Imtiaz and I had expected. (See figure 28.) M2D appeared to have calculated a voltage for the floating sample between 0 and 1, so that electric field lines pointed from objects of higher voltage to those of lower voltage. Furthermore, the electric field seemed to be strongest near the probe (especially between the tip and sample surface, although this wasn't obvious from the plot) and weakest far from any of the objects.

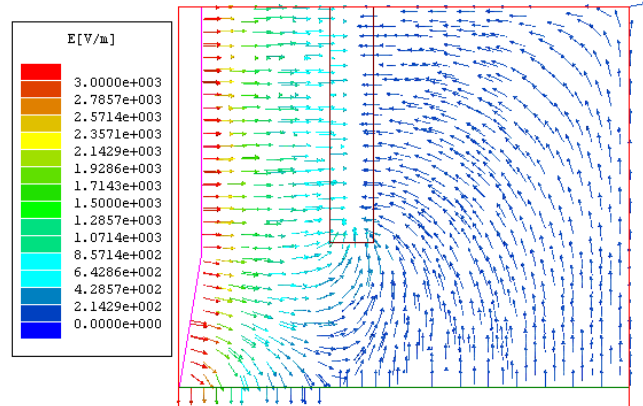


Figure 28. Vector plot of the electric field at $x=800 \mu\text{m}$ and $h=.5 \mu\text{m}$.

I was also interested in capacitances among the three conductors. I expected that as the separation between the probe and the sample increased, the capacitance between them would decrease. It would be reasonable to assume, therefore, that the capacitance between the probe and the outer conductor would increase (since electric field lines traveling from the probe to the sample at small h would now be redirected toward the outer conductor) while the capacitance between the sample and the outer conductor would decrease (since more electric field lines connect the probe to the outer conductor, requiring that fewer connect it to the sample).

In order to determine how capacitance depended on h , I plotted this relationship for capacitances among all three objects. (See figures 29–31.) The results for C_{p-o} and C_{o-s} appear to be well fit by lines of the form $a \cdot h + b$, where I varied a and b to minimize the errors.⁷ For C_{p-s} I used a natural logarithmic fit of the form $a \cdot \ln(h) + b$.⁸ All three capacitances depend on h as predicted.

It is not clear why the results for C_{p-o} and C_{o-s} would be linear, and, in fact, it is not entirely clear that these relationships are actually linear. They may instead merely appear to be linear for a certain range of h or for a small number of data points. However, the inverse logarithmic relationship between C_{p-s} and h is consistent with published literature.⁹

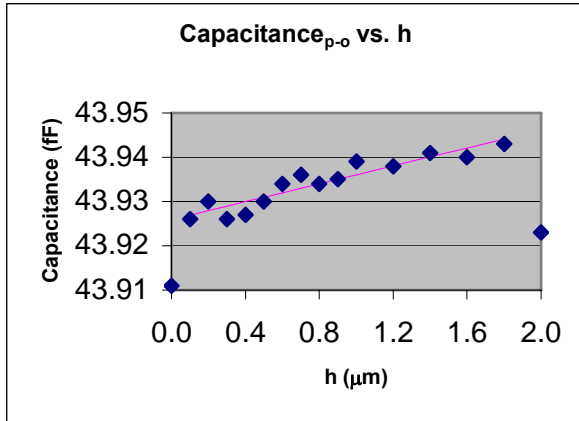


Figure 29. C_{p-o} at $x=800 \mu\text{m}$.

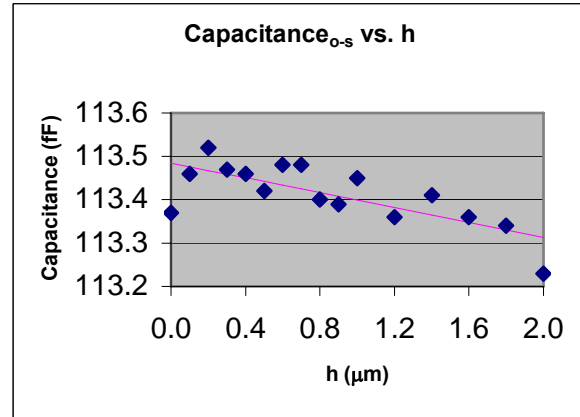


Figure 30. C_{o-s} at $x=800 \mu\text{m}$.

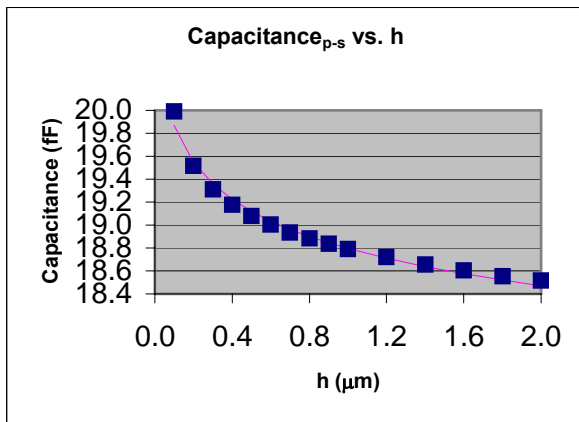


Figure 31. C_{p-s} at $x=800 \mu\text{m}$.

Changing the Geometry

⁷ I fitted this curve (and all curves in this thesis) by using the software program Excel to vary the independent fitting variables a_i so that z was a minimum, where $z = \sum (y_j - f_j)^2$, where the sum is taken from $j=1$ to n , n is the number of data points, y_j are the dependent values calculated by the software, $f_j = \sum a_i \cdot x_j^i$, this sum is taken from $i=1$ to p , x_j are the independent variable of the simulation, and where I determined p based on what I believed the dependence of f_j on x_j to be. In this case, $p=2$ so that the independent variables are a_1 and a_2 , y_j are the calculated values of capacitance, $n=16$ (since I ran the simulation for 16 values of h), and x_j are the values of h .

⁸ The value of C_{p-s} for $h=0 \mu\text{m}$ was 139.25 fF, although it is unusual to talk about the capacitance between two touching objects and it is impossible to take $\ln(0)$.

⁹ See the section “Sphere above a Plane” below.

Imtiaz was interested in whether changing the probe extension, x , would improve spatial resolution. I expected that if x decreased, then C_{p-o} would increase, since more of the outer conductor would be exposed, increasing the number of field lines that could extend to it from the probe; C_{o-s} would also increase, since the outer conductor and sample would be much closer to each other; and C_{p-s} would drop, since the probe and the outer conductor would send more field lines to the outer conductor, reducing the number that they could send to each other. By analogous reasoning, I expected that if x increased, then C_{p-o} would decrease, C_{o-s} would decrease, and C_{p-s} would increase.

First I ran a project with $x=100 \mu\text{m}$. I created a vector plot of the electric field for $h=.5 \mu\text{m}$, in which the behavior of the electric field lines appears to be qualitatively similar to their behavior in figure 28. (See figure 32.) It is interesting to note that because the outer conductor is closer to the sample surface, the electric field lines' bifurcation point (i.e., the point at which all lines to the left approach the sample and all points to the right depart from it) has shifted to the left, as the sample sends more such lines to the outer conductor than before. I again plotted capacitance as a function of h for capacitances among the three objects. C_{p-o} increased by about 5.5 fF (about 12.5%), C_{o-s} increased by about 250 fF (about 220%), and C_{p-s} dropped by about 5 fF (about 26%). These results confirmed my expectations.

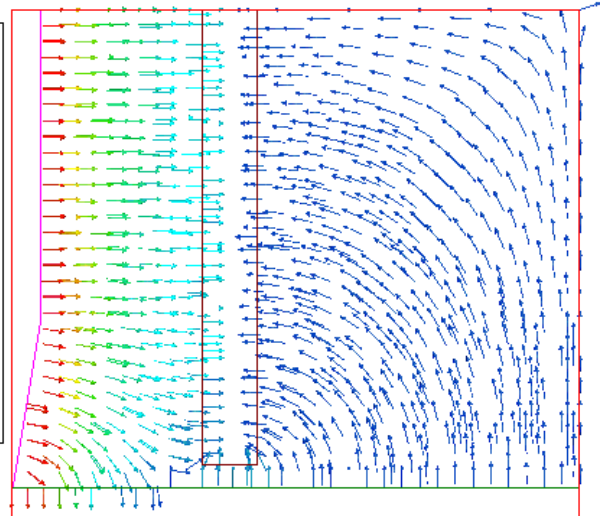
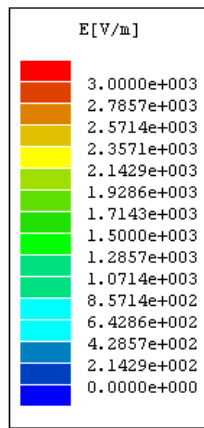


Figure 32. Vector plot of the electric field at $x=100 \mu\text{m}$ and $h=.5 \mu\text{m}$.

Next I let $x=2 \text{ mm}$. I created a vector plot of the electric field for $h=.5 \mu\text{m}$, and the behavior of the electric field lines appears again to be qualitatively similar to their behavior in figures 32 and 28, although their bifurcation point has now clearly shifted to the right since the outer conductor is far away. (See figure 33.) I again plotted capacitance as a function of h for capacitances among the three objects. In comparison with the $x=800 \mu\text{m}$ case, C_{p-o} has decreased by about 24 fF (about 55%), C_{o-s} has decreased by about 75 fF (about 65%), and C_{p-s} has increased by about 16 fF (about 85%). These results again confirmed my expectations.

Next I plotted the ratio of Z_s/Z_{p-o} and C_{p-s}/C_{o-s} for different values of x .¹⁰ (See figure 34.) Ideally both of these ratios would be small. Imtiaz's current geometry ($x=800 \mu\text{m}$) is clearly better than letting $x=2 \text{ mm}$, but it is not clear whether his spatial resolution would improve if he reduced x to about $100 \mu\text{m}$. In the end, Imtiaz decided to remain with his current microscope geometry.

¹⁰ In order to calculate Z_s/Z_{p-o} , I used the fact that impedance varies inversely with capacitance across a capacitor so that $Z_s/Z_{p-o}=C_{p-o}/C_s$.

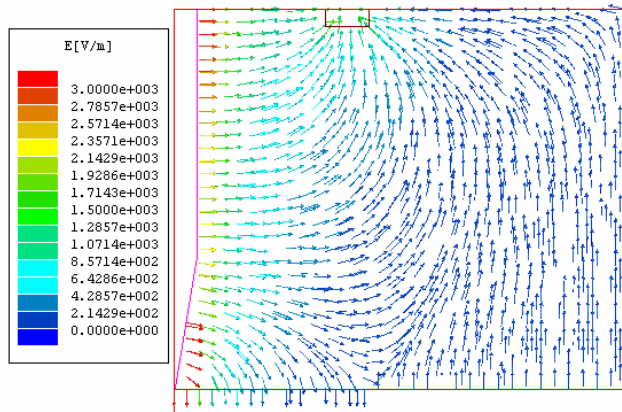


Figure 33. Vector plot of the electric field at $x=2$ mm and $h=.5 \mu\text{m}$.

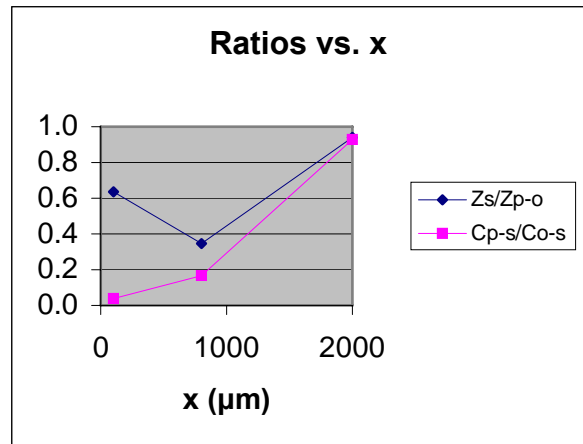


Figure 34.

Sphere above a Plane

Basis for Simulation

According to previous studies, treating microscopes like Imtiaz's microwave microscope as if they were spheres suspended above sample surfaces provides solutions that approximate experimental results.¹¹ Therefore, although it was only an approximation, for my next project I modeled the microscope tip by a sphere suspended above a conducting ground plane.

This problem can be solved analytically by using the image-charge method. A charge is placed at the center of the sphere, ensuring that the conducting sphere is at an equipotential of 1 V. In order to satisfy the symmetry condition across the sample surface, an image charge is placed on the opposite side of the surface. This induces another charge on the first side, and the process continues. Successive image charges are placed closer and closer to the surface, with successive iterations yielding more accurate results.

The resulting capacitance between the sphere and surface has been estimated as $C=4*\pi*\epsilon_0*R_0*\sinh(\alpha)*\sum(\sinh(n*\alpha))^{-1}$, where ϵ_0 is the permittivity of free space, R_0 is the radius of the sphere, $\alpha=\cosh^{-1}(1+h/R_0)$, h is the distance between the bottom of the sphere and the plane, and the sum is taken over all integers n from 1 to ∞ .¹² In the continuous limit, the sum may be converted to an integral, and the resulting expression can be estimated to give an inverse natural logarithmic dependence of capacitance on h (so that $C\approx k/\ln(h)$, where k is a constant), and Imtiaz expected to see this dependence in my results.

The Basic Project

I drew the model in M2D with $R_0=10 \mu\text{m}$. (See figure 35.) I ran the simulation for a range of values of h and plotted the results on a semilog scale. (See figure 36.) The purple line is a fitted curve of the form $C=a*\ln(h)+b$, where I varied the constants a and b to produce a best fit. The results appear to be roughly inverse logarithmic, as expected.

¹¹ Chen Gao *et al.*, "Quantitative Microwave Evanescent Microscopy," *Appl Phys Lett.* 75, no. 19 (8 November 1999), and Xiao-Dong Xiang and Chen Gao, "Scanning Evanescent Electro-magnetic Microscope," U.S. patent number 6,173,604 B1, 16 January 2001.

¹² Chen Gao *et al.*, "Quantitative Microwave Evanescent Microscopy," *Appl Phys Lett.* 75, no. 19 (8 November 1999).

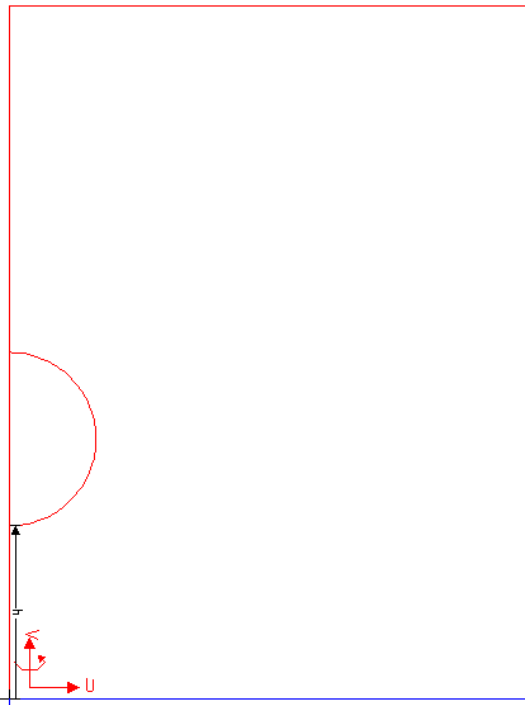


Figure 35.

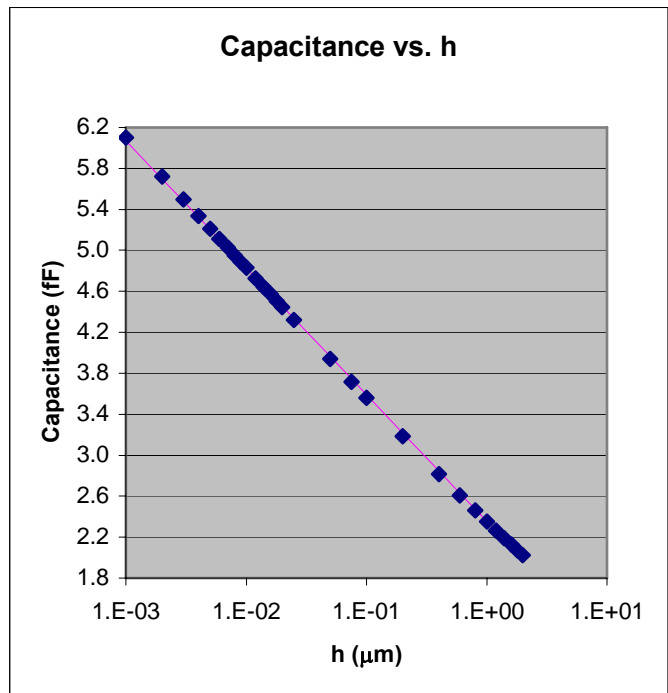


Figure 36.

After I ran this project, Imtiaz told me that he thought that a sphere of radius $37 \mu\text{m}$ would provide results that were closer to his experimental data. I therefore ran another project, with a sphere of radius $37 \mu\text{m}$. My data are represented by the red squares in figure 37. At the same time, Imtiaz calculated the expected capacitance using the software program Mathematica, using the image charge method for 1000 iterations. His results are represented by the blue diamonds in figure 37. The fitted lines for both sets of data points are of the form $C=a*\ln(h)+b$, as above.

Both sets of data exhibit an inverse logarithmic dependence, but their values are off by a few femtofarads. I thought that this might be because I drew the simulation model in a drawing area of only $60 \times 80 \mu\text{m}$. I imposed a Neumann boundary condition on the outer boundary of the model, requiring that electric field lines from the sphere to the sample had to remain within the drawing area. (See figure 38 for a demonstration of this effect.) I thought that this may have limited the number of field lines traveling from the sphere to the sample, reducing capacitance.

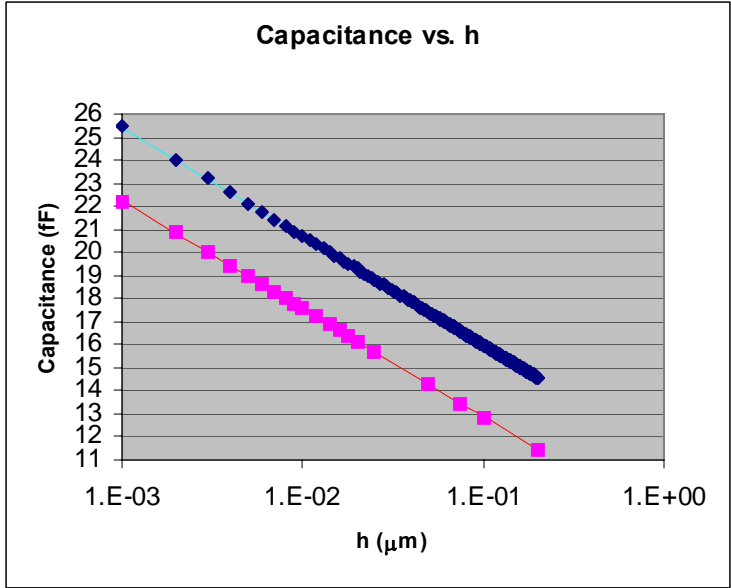


Figure 37.

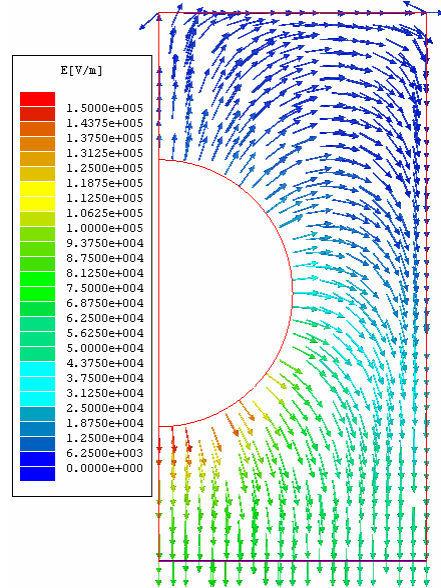


Figure 38. Electric field lines between a perfectly conducting sphere and plane with a Neumann outer boundary condition.

Therefore, I expanded the drawing area to 90 x 90 μm in order to see whether allowing more electric field lines would increase the calculated capacitance. My new data are represented by the green triangles in figure 39, which includes the previous simulation results and Imtiaz’s data. The new values of capacitance are greater than the previous ones and much closer to Imtiaz’s data. I assume that if I were able to run the project with an arbitrarily large box size, then my results would approach arbitrarily closely to Imtiaz’s data.

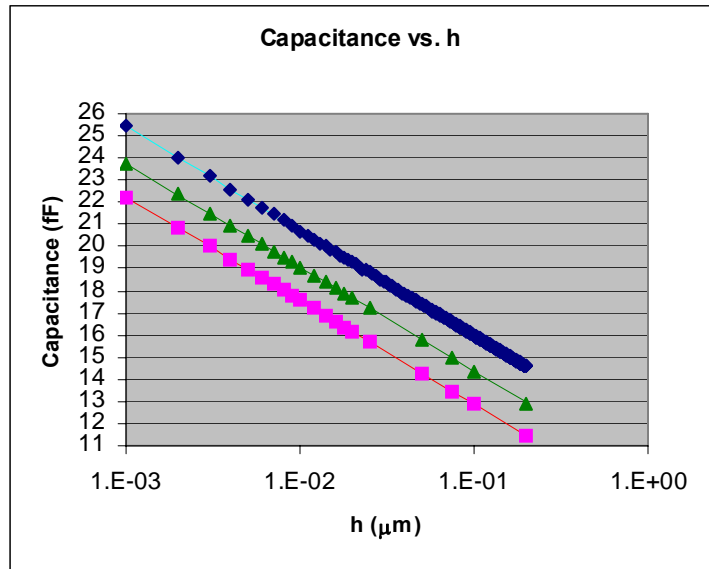


Figure 39.

With Perturbation

As the microscope tip is dragged along the sample surface, it can accumulate tiny particles of dirt. Imtiaz was interested in how these perturbations would affect the capacitance between the microscope tip and the sample. I simulated the perturbation by including a sphere of radius 150 nm directly below the primary sphere in the model. (See figure 40.) I defined h as the distance from the sample surface to the bottom of the perturbation sphere.

Imtiaz expected that the capacitance would no longer vary inverse logarithmically with height, especially at small distances, for which the perturbation should greatly affect the field structure between the two objects. However, he expected that the perturbation would have little effect at large distances, since in that case it would be much smaller than the area between the tip and the sample. Figure 41 presents results on a semilog scale.

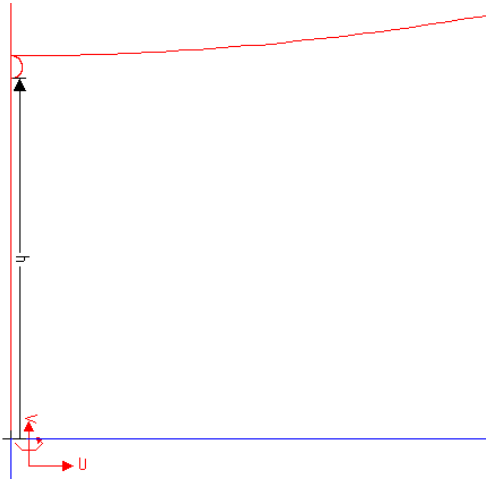


Figure 40. This is a blow-up of the area of the model between the spheres and the sample. The axis of rotational symmetry is the left edge. The area at the bottom, outlined in blue, is the sample. The bottom of the primary sphere is at the top of the figure, and the perturbation sphere is immediately below it.

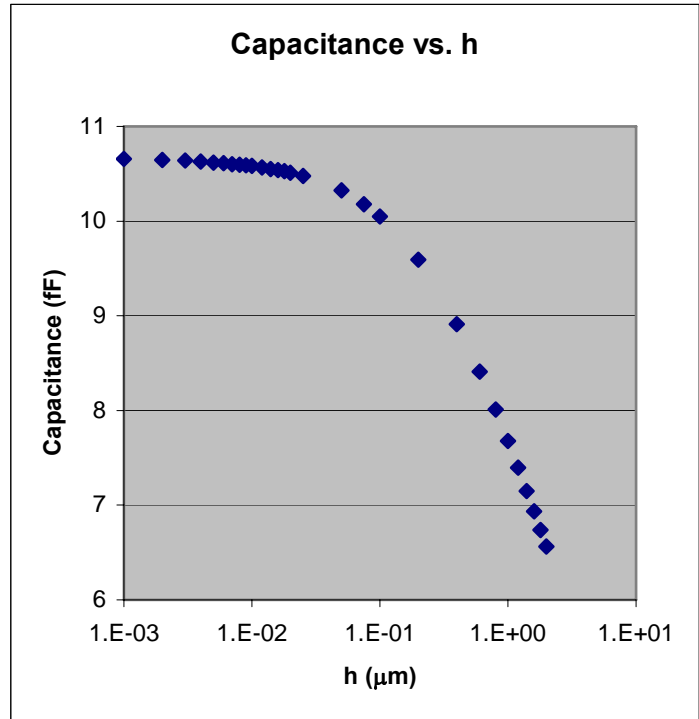


Figure 41.

The inverse logarithmic relationship between capacitance and height clearly breaks down when the spheres are near the sample. However, the relationship appears to hold when the spheres are far from the sample, indicating that the perturbation sphere has little effect in this case. It should be noted that Imtiaz did not calculate any expected values for the capacitance in Mathematica for this case, since the image charge method that he had used earlier was not valid with two spheres.

Sphere above a Plane with the Addition of a Thin Conducting Film

At the 2004 March meeting of the American Physical Society, Imtiaz heard another researcher claim that placing a thin metallic film above a substrate during microwave microscopy experiments could help to concentrate electric field lines near the tip. Imtiaz therefore asked me to simulate this kind of arrangement in order to verify the claim.

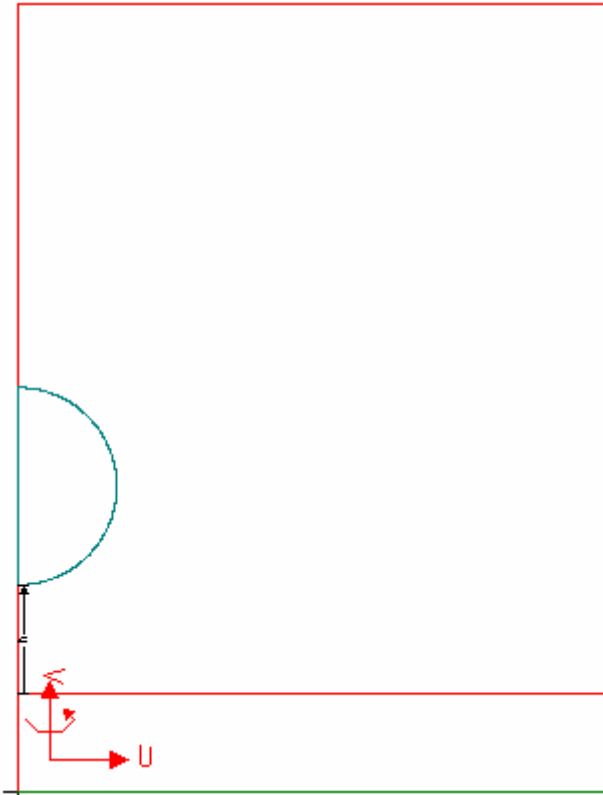


Figure 42. A conducting sphere above a dielectric substrate above a conducting ground.

I created the model in M2D. (See figure 42.) I drew a perfectly conducting sphere of radius $10\ \mu\text{m}$ (the blue semicircle) above a silicon substrate that was $10\ \mu\text{m}$ thick (the red rectangle near the bottom of the drawing area), which in turn was directly above a thin perfectly conducting ground layer (the very thin green rectangle at the bottom of the drawing area). I defined the distance between the sphere and the substrate to be h and varied this distance from $1\ \text{nm}$ to $1\ \mu\text{m}$. I assigned a voltage of $1\ \text{V}$ to the sphere and a voltage of $0\ \text{V}$ to the ground layer. After running that project, I replaced the topmost $.1\ \mu\text{m}$ of the substrate with a perfect conductor, which I let float, and ran that project.

I first plotted the magnitudes of the electric fields at $1\ \text{nm}$ for both projects. (See figures 43 and 44.) The field structures generally appeared to be nearly identical above the surface of the sample. (Below the surface, the presence of the perfectly conducting film induced a uniform electric field throughout the substrate.)

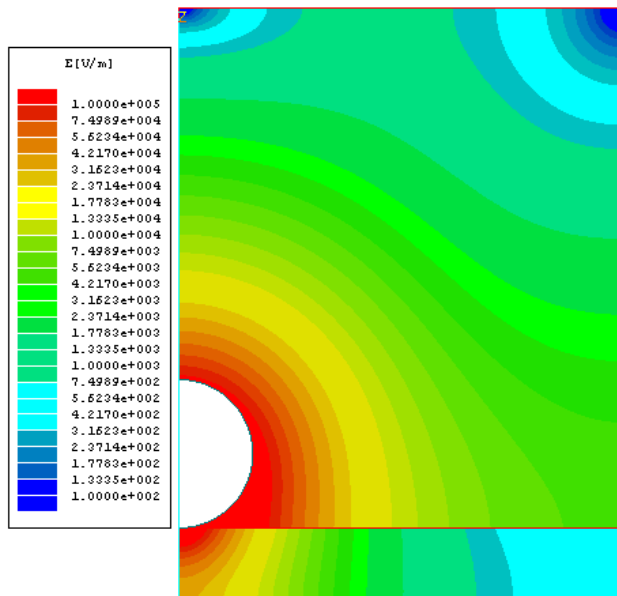


Figure 43. An electric field plot for a sphere above a substrate with no film, for $h=1\ \text{nm}$.

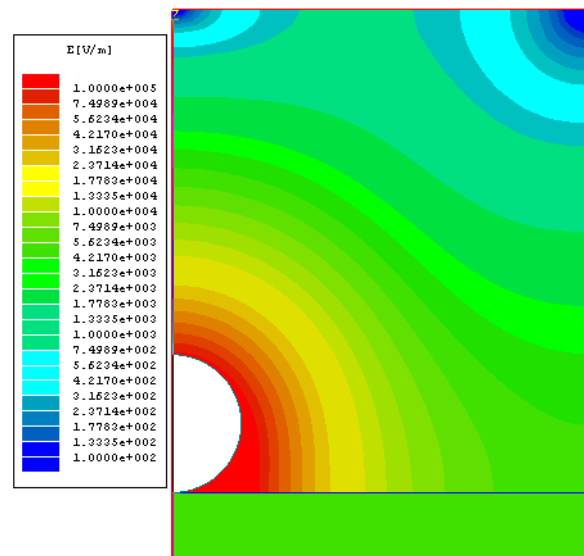


Figure 44. An electric field plot for a sphere above a substrate with a thin perfectly conducting film, for $h=1\ \text{nm}$.

However, the situation is very different in the gap directly between the sphere and the sample surface. (See figures 45 and 46.) Without the thin film at $h=1$ nm (figure 45), the magnitude of the electric field appears to be no greater than about 9.15×10^6 V/m near the axis of rotational symmetry, while with the film (figure 46), the magnitude of the electric field appears to be greater than 5×10^8 V/m in a region that extends much further from the axis. The thin film also appears to confine more of the electric field near the axis of rotation at $h=1$ μm , although the effect seems to be less pronounced at this height. (See figures 47 and 48.)

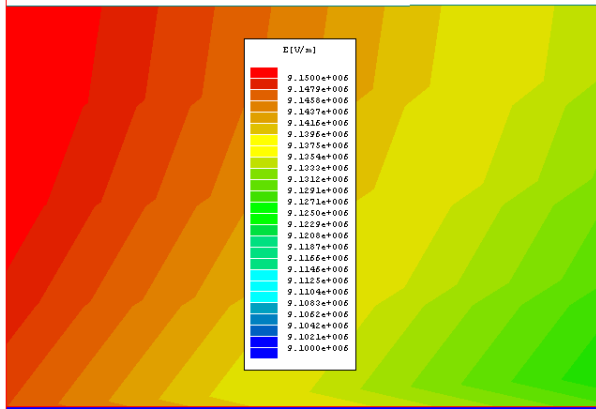


Figure 45. Electric field plot in the region immediately between a sphere and a silicon substrate for $h=1$ nm. The bottom of the sphere is at the very top of the figure, and the top of the substrate is at the very bottom. The axis of rotational symmetry is along the left edge.

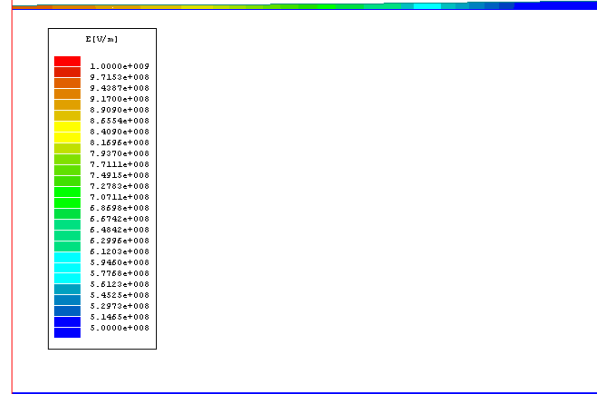


Figure 46. Electric field plot in the region immediately between a sphere and a perfectly conducting film above a silicon substrate for $h=1$ nm. The bottom of the sphere is at the very top of the figure, the film is the white area (.1 μm thick) that occupies most of the figure, and the top of the substrate is at the very bottom. The axis of rotational symmetry is along the left edge.

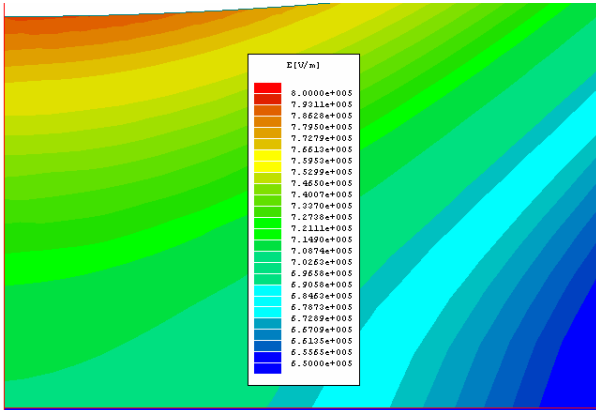


Figure 47. Electric field plot in the region immediately between a sphere and a silicon substrate for $h=1$ μm . The bottom of the sphere is at the very top of the figure, and the top of the substrate is at the very bottom. The axis of rotational symmetry is along the left edge.

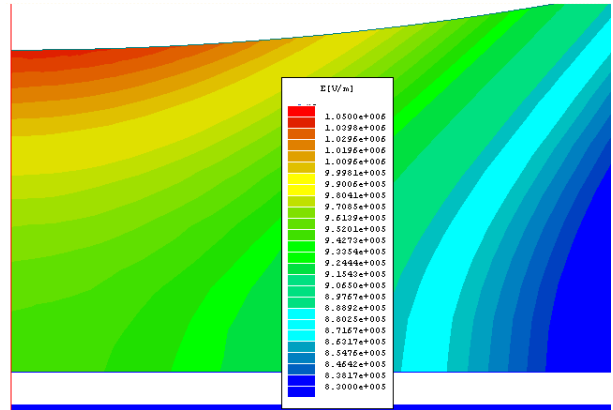


Figure 48. Electric field plot in the region immediately between a sphere and a perfectly conducting film above a silicon substrate for $h=1$ μm . The bottom of the sphere is at the top of the figure, the film is the white area near the bottom, and the top of the substrate is at the very bottom.

These results seem to demonstrate that when studying a sample with a microwave microscope, adding a thin film above a substrate can help to confine the field structure in the area directly underneath the tip, improving spatial resolution. If this is confirmed experimentally, this could help to improve the results of Imtiaz's experiments. However, it is important to note that these results are new (the simulations were completed in mid-April) and that we have not had time to study them thoroughly yet.

Conclusion

M2D simulations provided several insights into Imtiaz's microwave microscope experiments.

- First, they demonstrated that we could examine different microscope geometries and compare the extent to which they help to confine the field structure near the microscope tip.
- They showed that the spatial resolution of Imtiaz's current geometry is pretty good.
- Representing Imtiaz's microscope as a sphere provides results that are quite accurate. This can greatly simplify future simulations.
- Adding a perturbation to the bottom of a microscope tip destroys the inverse logarithmic dependence of capacitance on height. This suggests that if Imtiaz wants to take advantage of this mathematical relationship, then he must take great care to prevent the accumulation of dirt on his microscope tips.
- Finally, adding a thin film above a dielectric substrate may help to confine electric field structure during microwave microscopy experiments, greatly improving spatial resolution.

Glossary of Symbols

Symbol	Definition
ϵ_r	Relative electric permittivity
μ_r	Relative magnetic permeability
f	Frequency
h	Height of microscope probe tip above sample
n	Index of refraction
x	Height of outer conductor above microscope probe tip